International Journal of Mechanical Sciences 321 (2026) 111654

Contents lists available at ScienceDirect

International Journal of Mechanical Sciences

journal homepage: www.elsevier.com/locate/ijmecsci

High-Fidelity modeling of cold spray: Improved constitutive material model and nonlocal mesh sensitivity mitigation

Xuanyu Ge, Linglong Zhou, Sara Bagherifard, Mario Guagliano *

Politecnico di Milano, Department of Mechanical Engineering, Milan, Italy

ARTICLE INFO

Keywords:
Cold spray
Severe plastic deformation
Mesh sensitivity
Material model
Nonlocal method

ABSTRACT

Finite element method (FEM) is significantly helpful to simulate cold spray (CS) deposition for optimizing the process parameters or evaluating the deposit's physical and mechanical indexes. The simulations' accuracy, however, is primarily governed by the choice of constitutive material model, while also exhibiting notable sensitive to the mesh size. To enhance predictions and mitigate this sensitivity, here in, we developed an improved material model able to predict the deformation of the deposited particles with higher accuracy compared to the existing models. The model incorporates strain hardening, strain rate effects, and thermal softening into flow stress, utilizing a straightforward expression that facilitates implementation in FEM via a user-defined VUMAT subroutine and enables efficient experimental calibration. The impact of copper particles, as a representative material for CS, was simulated by the proposed model over a wide velocity range of 590–1058 m/s. The simulation results accurately reproduced the experimental particle deformation, local jetting and flatness, with predicted overlapping and flattening ratios exceeding 85% and 95% respectively, demonstrating a significant improvement over existing models at high impact velocities. Subsequent systematic simulations on mesh sensitivity revealed that the primary factors were the intrinsic kinematic issue from high-velocity impacts and the elliptic problem introduced by thermal softening. To address this sensitivity, a novel hybrid nonlocal strategy was introduced combining standard nonlocal and over-nonlocal methods. Specifically, the standard nonlocal method was utilized to mitigate the shear band localization, while the over-nonlocal method was leveraged to strongly regularize the temperature field. The proposed strategy was applied to CS simulations using various mesh sizes, showing its high efficiency in minimizing the effect of mesh size on both particle deformation and shear band localization.

1. Introduction

Cold spray (CS) is a solid-state coating deposition technique in which micro-sized particles are accelerated to high velocities (300–1200 m/s) using a compressed and pre-heated gas to impact a substrate and form a coating [1–3]. It has significant advantages such as high deposition rate [4], considerable deposit size and material flexibility [5] while avoiding residual stress typically associated with fusion-based manufacturing techniques [6]. These advantages make CS well suited for additive manufacturing [7] for a wide range of material groups (e.g. steel [8], copper [9], zinc [10] and ceramics [11]). Currently, one of the main challenges of CS is the tendency of its deposits to exhibit limited ductility [12], which restricts the potential application range of CS coated or manufactured components [13]. Although heat treatment can significantly improve the ductility of CS deposits [14,15], it somewhat deviates from the concept of rapid manufacturing [16,17]. Alternatively, recent studies by Li et al. showed that optimizing the spraying parameters can achieve both high strength and high ductility in as-sprayed Cu deposits [18,19]. Therefore, a thorough understanding of the CS bonding mechanisms is essential to ensure that the deposits meet the required mechanical properties.

Experimental exploration of the deposition mechanism can be costly and challenging due to the extremely small particle size [20] and their high impact velocity [21]. Studies have used high-speed cameras to capture the impact of single particles and determine the critical velocity [22,23]; however, the spatial and temporal resolution is still insufficient to fully understand the detailed variations during particle deposition. Other studies have employed electron microscopes to examine deposited particles and infer the deposition mechanisms based on their deformations [24]. Numerical simulations have been also widely used to

* Corresponding author.
E-mail address: mario.guagliano@polimi.it (M. Guagliano).

https://doi.org/10.1016/j.ijmecsci.2026.111654
Received 19 March 2026; Received in revised form 10 April 2026; Accepted 22 April 2026
Available online 24 April 2026

provide insight on this matter [25,26]. In numerical simulations of CS, a high-fidelity constitutive material model is essential for accurate predictions of particle deformation, as it provides a reliable benchmark to capture material behavior under extreme strain rates and thermal conditions. Such high precision at the single-particle level is a prerequisite for extending predictions to multi-particle interactions and full coating formation. The Johnson–Cook (JC) model [27] is the most classic and widely used in the field as it considers the effect of strain hardening, strain rate hardening and thermal softening on the flow stress. However, previous studies have demonstrated that the JC model tends to overestimate the deformation of CS deposited particles, as it is basically designed for lower strain rates ($<10^4$ s^{-1}) compared to what is typical in CS (10^7–10^9 s^{-1}) [28]. To address this, a modified JC model [29] along with several new material models [30,31] have been proposed to more accurately predict the deformation of CS deposited particles. Among them, the Ma-Wang (MW) model [26,28] recently became popular since it can be conveniently calibrated by experimental data, leading to deformed particle profiles reported to be in good agreement with the experimental data. However, when we used this model to predict the deformation of CS copper (Cu) particles at higher plastic strain range, the MW model showed some deviations from experimental data in capturing the overall deformation and local jetting of particles (see results in Section 3.4). Such high ranges of plastic strain can occur for impacting particles under very high velocities and also for the already deposited particles impacted by multiple upcoming particles.

Furthermore, accurate CS simulations depend not only on selecting an appropriate material model but also on effectively managing mesh size sensitivity in Eulerian formulations. The lack of standardized mesh sizing leads to variability in simulation outcomes, complicating reproducibility and reliability. Although a mesh size of 1/50th of the particle diameter has been commonly adopted and found to provide good simulation results [32], yet the predicted particle profiles are strongly sensitive to mesh size. This undoubtedly limits the reliability of CS simulations. On the one hand, when the simulation is extended to multi-particle impacts [33], the characteristics of the fixed Eulerian mesh lead to different mesh densities for different particle diameters [34,35], making the results further unconvincing. On the other hand, this loss of mesh uniqueness also impedes finding robust correlations between the deposit properties and simulation variables (e.g., adhesion strength and temperature [36]).

Our further investigation among high strain rate simulations has revealed that mesh sensitivity in CS simulations can mainly originate from two aspects: the intrinsic kinematic issue arising in high-velocity impact and the elliptic problem caused by thermal softening. Regarding the kinematic issue, the high velocity impacts cause intense local deformation and mesh distortion in the elements on the contact surface, thereby impeding the convergence of the Lagrangian approach [37]. The Eulerian formulation addresses this issue by fixing the Eulerian mesh and letting the material flow within it [38]. However, it essentially retains the basic characteristics of the Lagrangian mesh. During the simulation, the mesh first deforms to track material flow and then maps the simulated field to the original fixed mesh [39,40]. This phenomenon results in a kinematic issue at the contact interface during high-velocity impacts, which is particularly challenging to address due to the varying displacement and velocity responses produced by different Eulerian mesh sizes [41]. One possible solution for this is to improve the resolution of the coarse mesh by adopting high-order schemes originated from computational fluid dynamics [42], such as the weighted essentially non-oscillatory method [43]. However, this approach is overly complex and difficult to implement, because it involves modifying the mesh order, which is not permissible in the Abaqus Eulerian scheme. Therefore, a mechanical approach that can be implemented within the Eulerian framework seems more appropriate to mitigate this kinematic issue.

Regarding the elliptic problem, it commonly arises in constitutive material models that incorporate softening mechanisms, such as plastic or damage softening. In these situations, the material loses its ability to distribute deformation evenly, causing the deformation to become concentrated within a localized zone [44,45], which can eventually result in the emergence of shear bands [46] (a narrow zone of localized and intense plastic deformation) or cracks [33]. Similarly, when thermal softening is included in the constitutive material model, it can also lead to loss of ellipticity of the plastic deformation zone, especially in adiabatic shear simulations [41]. Several methods have been developed to regularize the thermal softening problem. Dolci et al. [47] regarded the Taylor-Quinney as a function of mechanical response and mesh size to regularize the temperature field. Luc et al. [48] applied heat diffusion to average the temperature field in shear bands. Nevertheless, these approaches were primarily intended for low velocity impacts and are therefore inadequate for simulating the high velocity impacts encountered in the CS process.

Nonlocal method is a strategy implemented to regularize the strain softening problem [49,50]. In this theory, one or several internal variables are determined by the spatial average of the associated field across their neighborhood, with a material length scale introduced to represent the volume affecting the nonlocal behavior [46]. Classic nonlocal method is generally time-consuming and difficult to apply to large-scale models, leading to the development of nonlocal implicit gradient enhancement [51,52], which introduces higher-order gradients of the local internal variables to avoid time-consuming nonlocal integrations [53,54]. This approach has been successfully integrated with plasticity [55] and damage models [56,57] to regularize boundary value problems. Although this method was not originally designed to regularize the temperature field, its theoretical generality seems suitable for addressing the elliptic problem caused by thermal softening in CS simulations.

To address the abovementioned challenges and enhance the quality of numerical simulations of the CS process, in this study, an improved high-fidelity material model was developed able to accurately predict the deformation behavior of the deposited particles. The new formula considers strain hardening, strain rate effects, and thermal softening on flow stress, yet remains straightforward, which makes it easy to implement in simulations and able to match with experimental data. The model was employed to simulate the CS processes of Cu particles across a broad velocity spectrum (590–1058 m/s). When benchmarked against experimental observations, the simulation results confirmed the model's enhanced predictive capability and fidelity in capturing particle deformation, local jetting and flattening ratio. Subsequently, a novel nonlocal strategy was proposed to mitigate the mesh sensitivity in the Eulerian CS simulations. In this strategy, the standard nonlocal method was applied to smooth shear band localization, while the over-nonlocal method was used to strongly regularize the thermal softening. The proposed hybrid nonlocal strategy was evaluated in CS simulations using different mesh sizes. The results showed that both particle deformation and shear band positioning remained nearly identical across different mesh sizes, demonstrating the high efficiency of the proposed strategy to mitigate mesh sensitivity.

The remainder of this paper is organized as follows. Section 2 introduces the proposed constitutive material model for CS simulations, followed by the numerical framework and single particle impact validation in Section 3. Mesh sensitivity in CS simulations is investigated in Section 4, while a nonlocal strategy is presented to alleviate its effects in Section 5. Finally, concluding remarks are given in Section 6.

2. Improved material model for CS simulation

Here, the overview of the proposed material model is introduced first in Section 2.1. Then, the comparison with the MW model is presented in Section 2.2.

2.1. Overview of the material model

To more accurately capture the deformation of CS deposited particles, an improved material model was developed as follows:

$$\sigma_y = \left[\underbrace{\left(\sigma_{y0} + A\varepsilon_p{}^n\right)}_{\text{Strainhardening}} + \underbrace{\left(\alpha\varepsilon_p{}^n+\beta\right)\ln\left(\frac{\dot{\varepsilon}_p}{\dot{\varepsilon}_s}\right)}_{\text{Normalstrainrate}} + \underbrace{B\ln\left(\frac{\dot{\varepsilon}_p}{\dot{\varepsilon}_u}\right)}_{\text{Highstrainrate}}\right]\underbrace{\left(\frac{1+e^{\left(T_r-T_{ref}\right)\eta}}{1+e^{\left(T-T_{ref}\right)\eta}}\right)}_{\text{Thermalsoftening}}, \tag{1}$$

where σ_y is the flow stress relying on the equivalent plastic strain ε_p, equivalent plastic strain rate $\dot{\varepsilon}_p$, and temperature T. It is compared with the von-Mises equivalent stress calculated under multiaxial stress states to determine whether the material yields. $\dot{\varepsilon}_s$ and $\dot{\varepsilon}_u$ are the reference equivalent plastic strain rates indicating the ranges of normal and high strain rate hardening, respectively.

For metals, the flow stress under high-velocity impact is mainly determined by three factors: strain hardening, strain rate hardening and thermal softening. Strain hardening captures the increase in flow stress with plastic deformation, while strain rate hardening reflects the strengthening effect at high strain rates. Thermal softening accounts for the reduction in flow stress due to heating. The combination of these three terms provides a physically meaningful framework that captures the competing hardening and softening mechanisms under extreme thermomechanical conditions. It originates from the classical JC model [27] and has subsequently been optimized or modified to address different problems [26,28,29]. Three terms and corresponding material parameters are discussed separately in the following Sections.

2.1.1. Strain hardening

When $\dot{\varepsilon}_p < \dot{\varepsilon}_s$, the material is under static or quasi-static loading conditions. Therefore, the flow stress is mainly affected by the equivalent plastic strain, and their relationship can be expressed in the following exponential form:

$$\sigma_y = \sigma_{y0} + A\varepsilon_p{}^n, \tag{2}$$

where σ_{y0} is the initial yield stress. A and n are the fitting parameters. This equation has been successfully used to describe the strain-hardening behavior of various metals, such as aluminum, Cu, iron, steel, titanium [26–29]. $\sigma_{y0} = 39$MPa, $A = 320$MPa and $n = 0.41$ provide a good fit for the flow stress of Cu at room temperature [28], as shown in Fig. 1(a).

2.1.2. Strain rate hardening

The normal and high strain rate terms are of primary importance as they can significantly affect the deformation of the deposited particles [28]. When $\dot{\varepsilon}_s \le \dot{\varepsilon}_p < \dot{\varepsilon}_u$, the flow stress exhibits a logarithmic relationship with the equivalent plastic strain rate, and it increases significantly with increasing the equivalent plastic strain. Thus, a new normal strain rate term is proposed here as:

$$\sigma_y = \left(\sigma_{y0} + A\varepsilon_p{}^n\right) + \left(\alpha\varepsilon_p{}^n + \beta\right)\ln\left(\frac{\dot{\varepsilon}_p}{\dot{\varepsilon}_s}\right), \tag{3}$$

where α and β are the fitting parameters to control the slope between the flow stress and normal strain rate. This slope can usually be expressed as a function of the equivalent plastic strain. Similar relationships can be

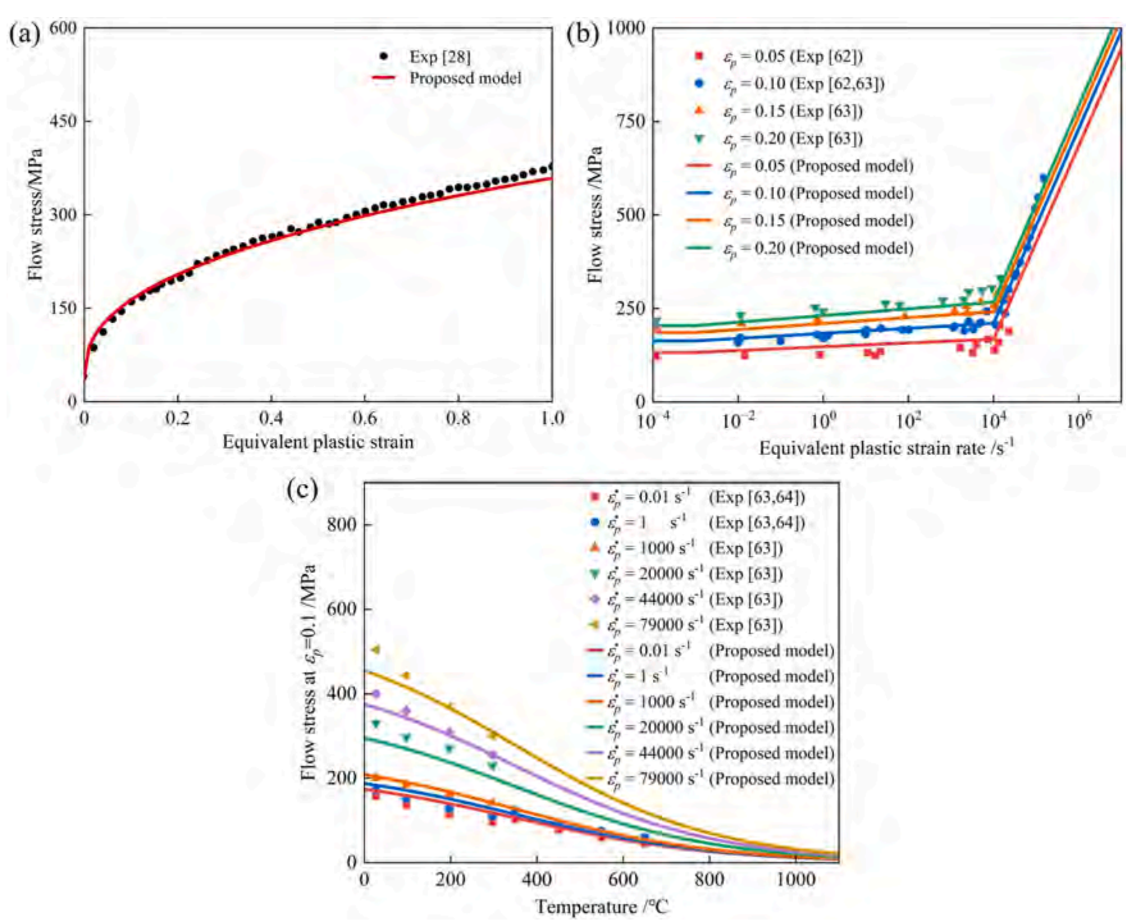

Fig. 1. (a) The flow stress–equivalent plastic strain curves of experimental data [28] and the proposed model under static or quasi-static loading conditions ($\dot{\varepsilon}_p < \dot{\varepsilon}_s$). (b) The flow stress–equivalent plastic strain rate curves of experimental data [62,63] and the proposed model at different equivalent plastic strains. (c) The flow stress–temperature curves of experimental data [63,64] and the proposed model at different equivalent plastic strain rates.

found in the JC model and its modified versions [27,29], and have been proven to be effective for a wide range of metals commonly used in CS [31–35]. Notably, the fitting parameters (e.g. α and β) introduced in the proposed model serve as indicators of the underlying mechanisms rather than direct physical quantities. They offer the capacity for straightforward calibration from experimental data ensuring the practical applicability of the semi-empirical model.

When $\dot{\varepsilon}_u \le \dot{\varepsilon}_p$, the flow stress increases steeply as the logarithm of the strain rate increases. A similar formula, in this case, was used in MW model [26,28], expressed as:

$$\sigma_y = \left\{ \underbrace{\left(\sigma_{y0} + A{\varepsilon_p}^n\right)}_{\text{Strainhardening}} + \underbrace{(\alpha\varepsilon_p + \beta)\left[1 - \frac{\sigma_{y0} + A{\varepsilon_p}^n}{\sigma_{cr}}\right]\ln\left(\frac{\dot{\varepsilon}_p}{\dot{\varepsilon}_s}\right)}_{\text{Normalstrainrate}} + \underbrace{B\ln\left(\frac{\dot{\varepsilon}_p}{\dot{\varepsilon}_u}\right)}_{\text{Highstrainrate}} \right\} \left[\underbrace{\frac{sigmoid\left(-\frac{T-T_a}{T_m-T_a}b\right)}{sigmoid\left(-\frac{T_r-T_a}{T_m-T_a}b\right)}}_{\text{Thermalsoftening}} \right]. \quad (6)$$

$$\sigma_y = \left(\sigma_{y0} + A{\varepsilon_p}^n\right) + \left(\alpha{\varepsilon_p}^n + \beta\right)\ln\left(\frac{\dot{\varepsilon}_p}{\dot{\varepsilon}_s}\right) + B\ln\left(\frac{\dot{\varepsilon}_p}{\dot{\varepsilon}_u}\right), \quad (4)$$

where B is the only fitting parameter to control the slope between flow stress and high strain rate. The transition in the hardening behavior of metals at high strain rates can be explained by dislocation theory [58], and such logarithmic relationship between flow stress and equivalent plastic strain rate has been broadly applicable to different metals [59–61].

Experimental relationships between flow stress and equivalent plastic strain rate taken from [62,63] were used to calibrate the proposed model at room temperature, considering the flow stress under different equivalent plastic strains. A good fit between the flow stress and the equivalent plastic strain rate of Cu was achieved at various equivalent plastic strains when considering $\alpha = 7.5$MPa, $\beta = 0.01$MPa, $\dot{\varepsilon}_s = 10^{-3}\text{s}^{-1}$, $B = 110$MPa and $\dot{\varepsilon}_u = 10^4\text{s}^{-1}$, as shown in Fig. 1(b).

2.1.3. Thermal softening

Within the temperature range from room temperature to the melting point, the flow stress of metals typically decreases as the temperature rises, showing an initial rapid rate of decrease, which later slows down [63]. Thus, the proposed model is suggesting the relationship between flow stress and temperature to be characterized by a logistic function, as described below:

$$\sigma_y = \left[\left(\sigma_{y0} + A{\varepsilon_p}^n\right) + \left(\alpha{\varepsilon_p}^n + \beta\right)\ln\left(\frac{\dot{\varepsilon}_p}{\dot{\varepsilon}_s}\right) + B\ln\left(\frac{\dot{\varepsilon}_p}{\dot{\varepsilon}_u}\right)\right]\left(\frac{1 + e^{\left(T_r - T_{ref}\right)\eta}}{1 + e^{\left(T - T_{ref}\right)\eta}}\right), \quad (5)$$

where T_r is the room temperature and is used to determine the beginning of thermal softening behavior. T_{ref} is the reference temperature where the decrease of flow stress is the steepest. η is a fitting parameter to determine the rate of decrease of the flow stress and is assumed to vary with equivalent plastic strain rate [63], but for some metals, it can be treated as a constant for simplicity. The formula is normalized to ensure that the thermal softening term equals 1 at room temperature. The experimental flow stress–temperature data at different equivalent plastic strain rates were used to calibrate the formulation [63,64], with $T_{ref} = 350^\circ$C and $\eta = 4.3 \times 10^{-3\circ}\text{C}^{-1}$ providing the best fit, as shown in Fig. 1(c). The logistic function provides an effective empirical fit; although it does not explicitly capture the underlying microphysical mechanisms, it has been proven to effectively describe the softening behavior of most metals used in CS [26,28,65,66], demonstrating its broad applicability.

2.2. Comparison with the MW model

To better demonstrate the efficiency of the proposed model, a direct comparison is made with the MW model that was previously suggested for CS simulation [28]. The formula of MW model is expressed as:

As noted by comparing Eq. (1) and Eq. (6), the main difference is that the proposed model modified the normal strain rate and thermal softening terms. For the normal strain rate term, the exponent of equivalent plastic strain was used, which makes the flow stress of the proposed model lower than that of the MW model at high equivalent plastic strains. As regards the thermal softening term, the proposed model considered the relationship between flow stress and temperature at different equivalent plastic strain rates. This causes the flow stress of the proposed model to decrease more rapidly than that of the MW model at high equivalent plastic strain rates, better reflecting the rapid decrease of thermal softening.

3. Prediction of the deposited particles' deformation for various velocities

This section begins with a description of the finite element model and numerical framework in Section 3.1, followed by the implementation of the proposed constitutive model in Section 3.2. The simulation setup is introduced in Section 3.3, and the results and their comparison with experimental data are discussed in Section 3.4.

3.1. Finite element model development

The Eulerian framework [67–70] was applied in the Abaqus software to simulate a single Cu particle deposition on a Cu substrate as shown in Fig. 2. The contact of Eulerian scheme in Abaqus is a default, non-modifiable setting that provides a robust and stable treatment of particle–substrate interactions [68–70]. The Eulerian domain was considered as a cube with a length of 100 μm to mitigate the effect of reflected shear waves. A finer mesh was applied at the impact region with the element size of $h = 1/50$th of the particle diameter, while a coarser mesh was used elsewhere, following a gradient strategy. Additionally, the 1/4th of model was employed to reduce computational cost. Symmetric boundary conditions were applied to the symmetry surfaces, and the bottom side of the substrate was fully constrained. Notably, although particle diameter and shape can affect deformation behavior, with larger particles exhibiting higher inertial effects and non-spherical geometries leading to asymmetric deformation, only spherical particle with a diameter of 10 μm was considered, which aligns with the experimental conditions reported by Tiamiyu et al. [71,72] to ensure a direct and rigorous validation of the proposed model.

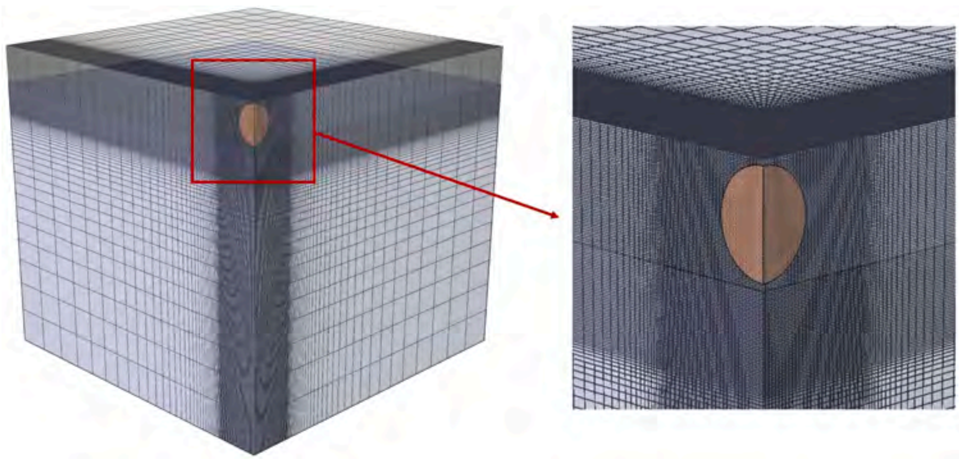

Fig. 2. Mesh distribution and the geometry of the Eulerian model for simulating single particle deposition.

3.2. Numerical implementation of the proposed model

The implementation of the proposed model was based on a user-defined material (VUMAT) subroutine. J_2 plasticity with isotropic hardening was considered, where yielding is governed by the second invariant of the deviatoric stress tensor. The return mapping algorithm [73] was applied to compute the plastic multiplier γ, which determines the magnitude of plastic flow during the stress update. The following formulas are utilized to determine whether plastic yielding occurs:

$$f = \sqrt{\frac{3}{2}\boldsymbol{\sigma}_{dev} : \boldsymbol{\sigma}_{dev}} - \sigma_y \text{with} \boldsymbol{\sigma}_{dev} = \boldsymbol{\sigma} - \frac{1}{3}tr(\boldsymbol{\sigma})\mathbf{I}, \tag{7}$$

where $\boldsymbol{\sigma}_{dev}$ and $\boldsymbol{\sigma}$ are the deviatoric stress tensor and the Cauchy stress tensor, respectively. Compared with quasi-static plastic problems, the challenge in implementing the proposed model lies in the requirement to simultaneously calculate three variables: ε_p, $\dot{\varepsilon}_p$ and T, that simultaneously affect the flow stress during plastic correction. They can be updated as follows:

$$\begin{aligned}\varepsilon_{p,n+1} = \varepsilon_{p,n} + \sqrt{\frac{2}{3}}\gamma_{n+1}, \dot{\varepsilon}_{p,n+1} = \sqrt{\frac{2}{3}}\dot{\gamma}_{n+1} \text{and} T_{n+1} \\ = T_n + \sqrt{\frac{2}{3}}\left[\frac{\gamma_{n+1}\left(\sigma_{y,n+1} + \sigma_{y,n}\right)}{2}\right]\frac{Q}{\rho c_p},\end{aligned} \tag{8}$$

where Q is the Taylor-Quinney coefficient defining the ratio of plastic energy converted into heat energy. This parameter must be obtained from experiments since its value can vary notably across different metals [74,75]. ρ is the density of material and c_p is the specific heat coefficient.

The Newton–Raphson method was employed to iteratively calculate γ. The bisection method was used after each iteration to update the interval. When the iteration was out of the interval, the initial guess was repositioned to improve the robustness. More details about this methodology can be found in [76], regarding VUMAT implementation of elastoplastic constitutive laws in FEM.

Due to the extremely rapid nature of the CS deposition process, many prior investigations have adopted the adiabatic approximation [26,28,34,36], employing Eq. (8) to estimate the resulting temperature increase.

When heat diffusion is considered, the temperature field will be computed by Abaqus's built-in module, and only the inelastic dissipation energy $W^{Inelastic}$ needs to be defined in the VUMAT subroutine, as follows:

$$W^{Inelastic}_{n+1} = W^{Inelastic}_{n} + \sqrt{\frac{2}{3}}\frac{\gamma_{n+1}\left(\sigma_{y,n+1} + \sigma_{y,n}\right)}{2\rho}. \tag{9}$$

A flowchart of the numerical implementation of the proposed constitutive material model is provided in Appendix B. To make a realistic simulation, heat diffusion was applied in all models described in Section 3.4.

3.3. Simulation settings and material properties

The particle and the substrate were set to 25 °C, as in the experiments [71,72]. Six different flight velocities were considered for the particle, namely: 590 m/s, 605 m/s, 768 m/s, 918 m/s, 990 m/s and 1058 m/s, following the experimentally measured velocities in [71,72]. The total step time of the simulations was set to 2.5 × 10^{-8} s. Thermal-displacement analysis step and Eulerian 8-node thermally coupled reduced-integration solid element (EC3D8RT) were utilized to calculate the temperature field. The default artificial viscosity was adopted, as it has been widely demonstrated to effectively maintain numerical stability and accuracy [38,68–70]. Simulations were conducted using both the proposed model and the MW model for comparison. The material properties of Cu are detailed in Table 1. Table 2 presents a comprehensive comparison of the material parameters employed in both the proposed model and the MW model.

3.4. Simulation results

A comparative analysis of the experimentally observed morphologies of deposited particles and the simulation results obtained from both the proposed material model and the MW model at various impact velocities is presented in Fig. 3. All simulation results in this study are extracted after elastic recovery at the end of deposition. It is worth noting that the proposed model in this study was compared only with the MW model to highlight its performance, since the MW model has been demonstrated to exhibit relatively high accuracy at low velocities, compared to the widely used JC model [27].

Overall observation indicated that the proposed model demonstrated strong accuracy in replicating the deformation of CS deposited Cu particles across a broad range of impact velocities (590–1058 m/s) observed experimentally [71,72]. By comparison, the MW model demonstrated reliable predictions of particle deformation solely at the

Table 1
Material parameters considered for the Cu particles [28,74,75].

Young's modulus E (GPa)	128
Poisson's ratio ν	0.34
Density ρ (kg/m^3)	8960
Specific heat c_p (J·kg^{-1}· °C^{-1})	384.6
Conductivity k (W·m^{-1}· °C^{-1})	385
Taylor-Quinney coefficient Q	0.75

Table 2
Material parameters of the proposed model and the MW model.

Proposed model [28,62–64]		MW model [28]	
σ_{y0} (MPa)	39	σ_{y0} (MPa)	39
A (MPa)	320	A (MPa)	320
n	0.41	n	0.41
α (MPa)	7.5	α (MPa)	17.5
β (MPa)	0.01	β (MPa)	0.1
$\dot{\varepsilon}_s$ (s^{-1})	0.001	$\dot{\varepsilon}_s$ (s^{-1})	0.001
$\dot{\varepsilon}_u$ (s^{-1})	10,000	$\dot{\varepsilon}_u$ (s^{-1})	7000
B (MPa)	110	σ_{cr} (MPa)	1500
T_{ref} (°C)	350	B (MPa)	110
η (°C^{-1})	0.0043	T_a (°C)	698.1
/	/	b	1.76
/	/	T_m (°C)	1084

lower impact velocities of 590 m/s and 605 m/s. For both models, as the impact velocity increased, the particles progressively penetrated the substrate, causing significant jetting at the particle edges. Consistent with previous studies [28], the maximum equivalent plastic strain was always concentrated in the jetting region along the particle–substrate interface, which is also reported as the typical location with the highest adhesion strength [77].

The profiles of the particles and substrate were extracted from both experiments and simulations for further comparison, as presented in Fig. 4. Since the experimental particle profiles were acquired at a stage tilt angle of 52°, the simulation contours were also rotated by the same angle to extract comparable profiles. The results show that the proposed material model can not only better predict the overall particle deformation, but also more accurately capture the localized jetting induced by thermal softening. Compared to the MW model, particle profiles obtained by the proposed model have flatter morphology and more pronounced jetting. Moreover, the proposed model predicted a higher penetration depth at the velocity range of 768–1058 m/s. The more accurate prediction of CS deposited Cu particles by the proposed material model can be attributed to the lower flow stress at higher equivalent plastic strains, and the stronger thermal softening at high equivalent plastic strain rates of this model.

To quantitatively evaluate the accuracy of the proposed material model, the overlapping ratios between the simulated particle area and the experimental particle area at different impact velocities were calculated by Eq. (10):

$$\text{Overlappingratio} = \frac{\text{Overlappingparticlearea}}{\text{Experimentalparticlearea}}. \tag{10}$$

The results shown in Fig. 5(a) demonstrate the high precision of the proposed model, which achieves the maximum overlapping ratio of 96.3% at 590 m/s and the minimum of 85.6% at 990 m/s. Throughout the entire velocity range, the proposed model outperforms the MW model in predictive accuracy. The deviation between the two models becomes more significant at higher velocities (>900 m/s); for example, at 1058 m/s, the proposed model reaches an overlapping ratio of 93.2%, whereas the MW model drops significantly to 61.8%.

As an additional comparison index, flattening ratios (described in Eq. (11)) of the particles were also calculated at different impact velocities by [71]:

$$\text{Flatteningratio} = \ln\left(\frac{\text{Particlediameter}}{\text{Deformedparticleheight}}\right). \tag{11}$$

Comparison between the flattening ratios of experimental and simulated data obtained using the proposed model are shown in Fig. 5 (b). The predicted flattening ratios show excellent correlation with experimental values, with relative deviations remaining below 5%. As the velocity increased from 590 m/s to 1058 m/s, the flattening ratio of the deposited Cu particles increased from approximately 0.4 to 0.6, which is an expected trend due to the increased particle deformation induced by higher kinetic energy.

4. Mesh sensitivity in CS simulation

Besides material model, the choice of element size is also of utmost importance in defining the accuracy of FEM models. The appropriate mesh size for the Eulerian simulations of CS process has never reached a unified agreement. Although, as shown in Section 3, a mesh size of $h =$ 1/50th of particle diameter is commonly used by researchers and shown to provide good simulation results, still the deformation of CS deposited particles is quite dependent on the mesh size. Therefore, here we systematically investigated the mesh sensitivity in CS simulations. Section 4.1 focuses on the kinematic issue associated with high velocity impact, while Section 4.2 examines the mesh sensitivity arising from thermal softening.

Three different approaches (i) without thermal softening, (ii) adiabatic and (iii) heat diffusion were used to study the mesh sensitivity issues associated with the kinematic aspects and thermal softening. For each approach, three representative velocities (590 m/s, 918 m/s and 1058 m/s) along with three mesh sizes ($h = 1/25$th, $h = 1/50$th and $h =$ 1/100th of particle diameter) were considered. The same simulation setting in Section 3 was used. Temperature evolution during the impact process obtained from different simulation approaches is provided in Appendix C.

4.1. Kinematic issue

In CS simulations, the specific elements residing at the particle-substrate interface are considered to have a displacement of u and velocity of v at any increment, as shown in Fig. 6. Since the edges of these EC3D8RT elements cannot bend, we assume a worst-case scenario where the deformation is entirely exerted to the elements adjacent to the interface. In this scenario, the width of the shear band observed in the fine mesh is reduced to half that in the coarse mesh. Consequently, both the equivalent plastic strain and the equivalent plastic strain rate within the shear band are doubled in the fine mesh compared to the coarse mesh. This scenario illustrates the underlying mechanism of the kinematic issue associated with high-velocity impacts, where mesh refinement leads to localized intensification of deformation parameters, thereby affecting the fidelity and stability of the simulation results.

The proposed model was used to verify this kinematic issue without considering the effect of thermal softening. The simulation results (see Fig. 7) indicate that the finer mesh leads to a significantly narrower shear band and an increased maximum equivalent plastic strain at all velocities. At a velocity of 590 m/s, particle deformation was roughly the same across different mesh sizes. Whereas at velocities of 918 m/s and 1058 m/s, deformation at the particle edges was more pronounced for the finer mesh. These results indicate that the kinematic issue has a significant influence on the mesh sensitivity in CS simulations.

4.2. Elliptic problem

There are two commonly used approaches in CS simulation: adiabatic [28,78] and heat diffusion [33]. In adiabatic analysis, the temperature field depends entirely on the equivalent plastic strain, meaning that the temperature distribution matches the equivalent plastic strain field. In contrast, heat diffusion analysis considers heat conduction, so the heat is not only concentrated in the shear band but can also be transferred to regions with lower temperatures.

Herein, first, the simulations were conducted using adiabatic analysis (see Fig. 8). The results indicated that at all velocities, particle deformation varied significantly across different mesh sizes. This is caused by the loss of ellipticity resulting from thermal softening. As the mesh is refined, equivalent plastic strain and temperature increase, leading to a decrease in the flow stress, which in turn makes it easier for the elements within the adiabatic shear band to deform, and thus leads

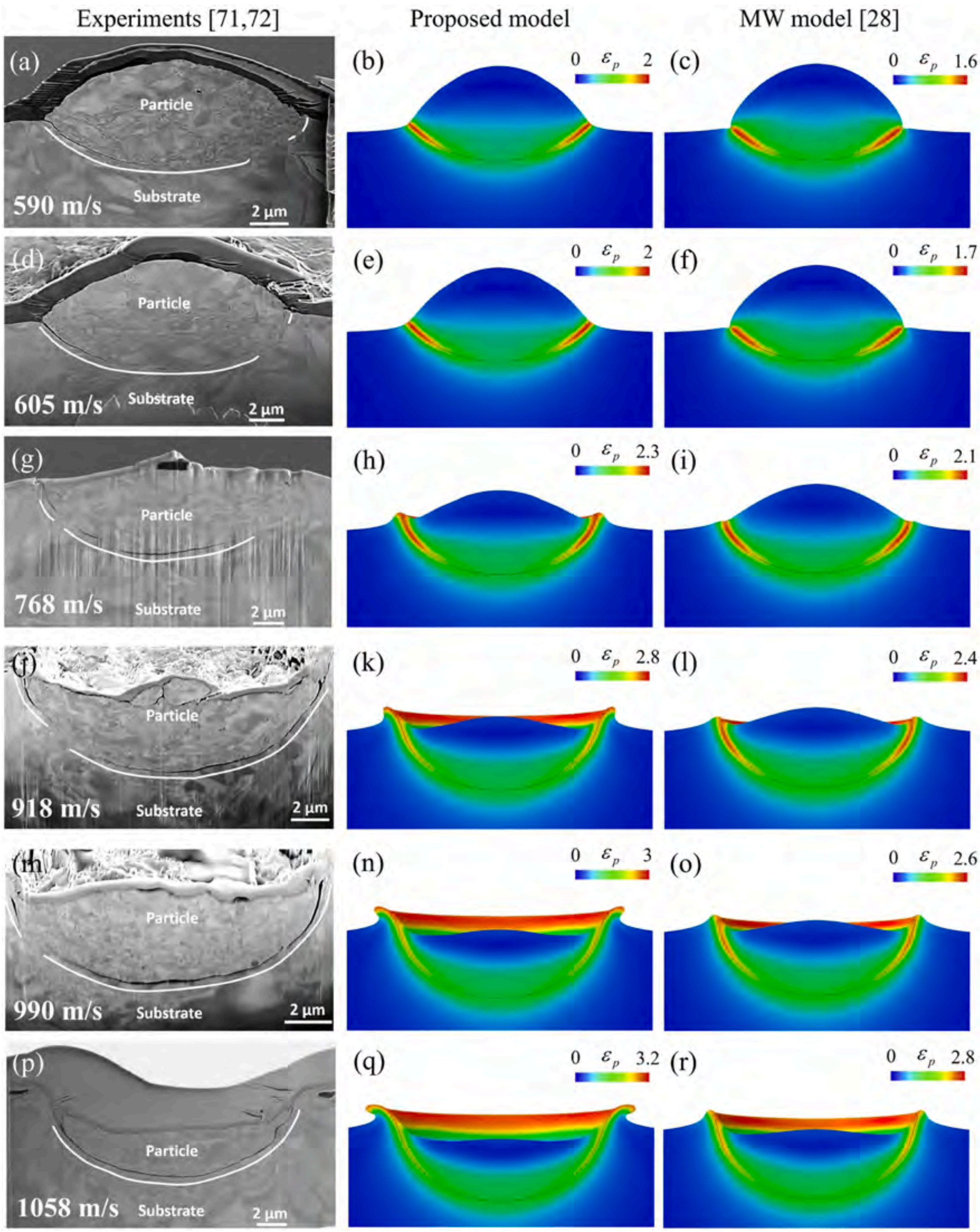

Fig. 3. Comparison between the experimental morphologies and the simulation results (both the proposed material model and MW material model) at different impact velocities of: (a-c) 590 m/s; (d-f) 605 m/s; (g-i) 768 m/s; (f-l) 918 m/s; (m-o) 990 m/s; (p-r) 1058 m/s. The contours represent the equivalent plastic strain field.

to further increase in equivalent plastic strain and temperature. Compared with the results of the analysis where thermal softening was neglected (Fig. 7), adiabatic analysis significantly increased the mesh sensitivity, resulting in a narrower shear band and more severe particle deformation, as the element size decreased. Especially for the mesh size of $h = 1/100$th of particle diameter, an excessively exaggerated jetting can be observed in Fig. 8(c), (F) and (i).

Moreover, since heat was concentrated in the shear band during adiabatic analysis, unrealistic melting occurred at velocities of 918 m/s and 1058 m/s with the mesh size of $h = 1/100$th particle diameter, as shown in Fig. 9(a) and (b), respectively.

Another set of simulations were conducted using heat diffusion analysis, the results of which are presented in Fig. 10. In these simulations, particle deformations were suppressed compared with adiabatic analysis. Especially at the velocity of 590 m/s, almost identical particle deformations were noted across different mesh sizes (see Fig. 10(a), (b) and (c)). This observation can be attributed to the fact that the heat transferred away from the adiabatic shear band can mitigate the effect of thermal softening on the flow stress. However, compared with the analysis where thermal softening was neglected at velocities of 918 m/s

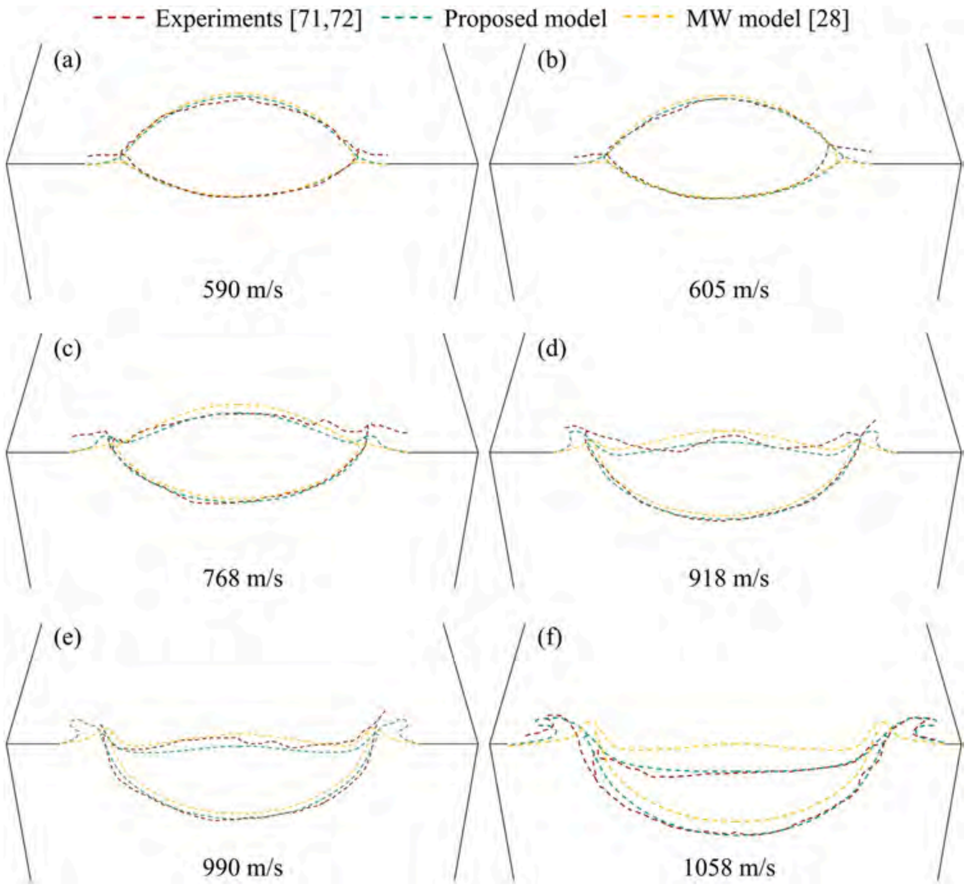

Fig. 4. Overlapped particle profiles for comparison between the experimental data and the simulated results (both the proposed model and MW model) at different impact velocities of: (a) 590 m/s; (b) 605 m/s; (c) 768 m/s; (d) 918 m/s; (e) 990 m/s; (f) 1058 m/s.

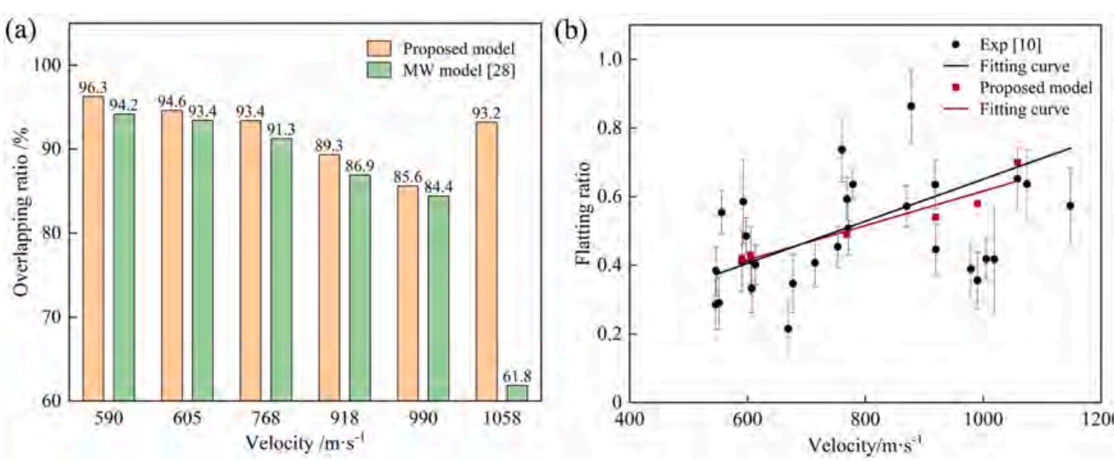

Fig. 5. (a) Overlapping ratio of CS deposited Cu particles obtained from the proposed model and MW model compared with experimental data [28]. (b) Flattening ratio of CS deposited Cu particles obtained from experiments [71] and the simulations using the proposed model.

and 1058 m/s with the mesh size of $h = 1/100\text{th}\ d$ (see Fig. 7(f) and (i)), excessive jetting could still be observed in Fig. 10(f) and (i); moreover, an unrealistic melting occurred at 1058 m/s, as demonstrated in Fig. 9 (c). This is because heat cannot be fully transferred out of the adiabatic shear band in high velocity impacts, leading to excessive deformation in the finer mesh.

In summary, both adiabatic and heat diffusion analyses make CS simulations more sensitive to mesh size, resulting in particle deformations that vary with element size and are not unique. Additionally, material properties can also affect mesh sensitivity. Specifically, the parameters governing strain rate and thermal softening may influence the intensity of localization, thereby indirectly impacting mesh dependence.

5. Nonlocal strategy to mitigate mesh sensitivity

Based on the investigation in Section 4, the nonlocal theory is first introduced in Section 5.1. Then, the development and numerical implementation of the proposed nonlocal strategy are presented in Sections 5.2 and 5.3. The corresponding simulation results are discussed

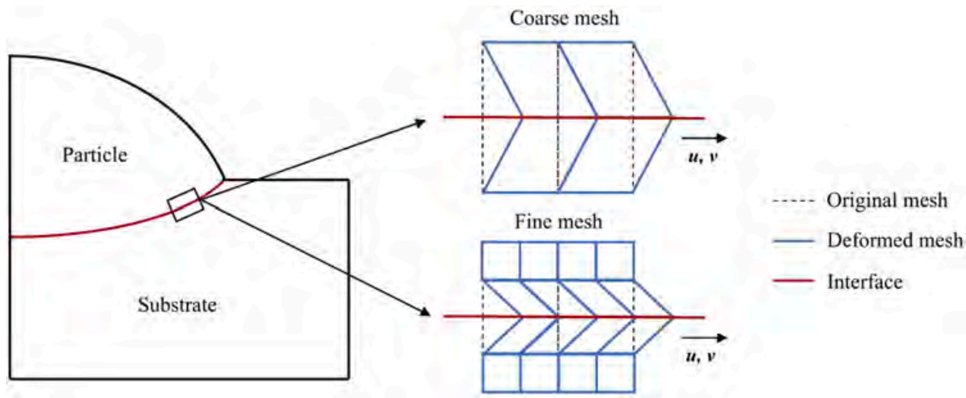

Fig.6. Deformation of elements at the interface for coarse and fine meshes.

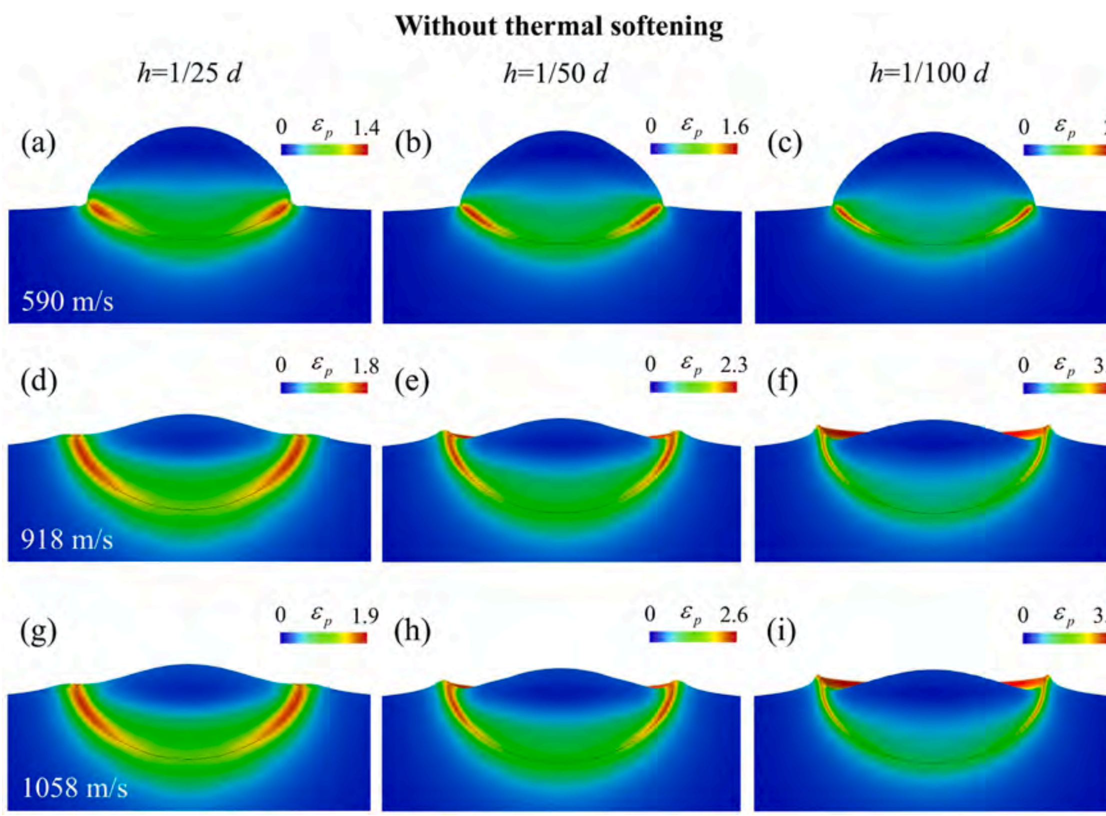

Fig. 7. Particle deformation and equivalent plastic strain field under different velocities and mesh sizes simulated by the proposed model while neglecting the thermal softening term.

in Section 5.4.

5.1. Nonlocal theory

Nonlocal methods are widely used to address the mesh sensitivity problem in constitutive material models with softening behavior [45]. In the classical nonlocal formulation, the local variable $f(\mathrm{x})$ is replaced by its spatial average $\bar{f}(\mathrm{x})$ [79]:

$$\bar{f}(\mathrm{x}) = \frac{\int_V w(\mathrm{x},\mathrm{y}) f(\mathrm{x}) dv}{\int_V w(\mathrm{x},\mathrm{y}) dv}, \tag{12}$$

where x and y are the coordinate vectors, $w(\mathrm{x}, \mathrm{y})$ is the weight function and V is the nonlocal integration domain. Classical nonlocal methods are time-consuming and not suitable for CS simulations. To overcome this limitation, gradient approximations of the nonlocal integral formulation were developed [51], to approximate the evolution of the local variable f (y) by Taylor's expansion:

$$\begin{aligned} f(\mathrm{y}) = {} & f(\mathrm{x}) + (y_i - x_i)\frac{\partial f}{\partial x_i} + \frac{(y_i - x_i)\left(y_j - x_j\right)}{2!}\frac{\partial^2 f}{\partial x_i \partial x_j} \\ & + \frac{(y_i - x_i)\left(y_j - x_j\right)(y_k - x_k)}{3!}\frac{\partial^3 f}{\partial x_i \partial x_j \partial x_k} + \cdots \end{aligned}. \tag{13}$$

Assuming that $w(\mathrm{x}, \mathrm{y})$ is isotropic over the nonlocal domain, the odd derivatives will vanish when $f(\mathrm{y})$ is substituted into Eq. (12). Then, the gradient form of the nonlocal variable can be obtained as:

$$\bar{f}(\mathrm{x}) = f(\mathrm{x}) + C_1 \nabla^2 f(\mathrm{x}) + C_2 \nabla^4 f(\mathrm{x}) + \cdots, \tag{14}$$

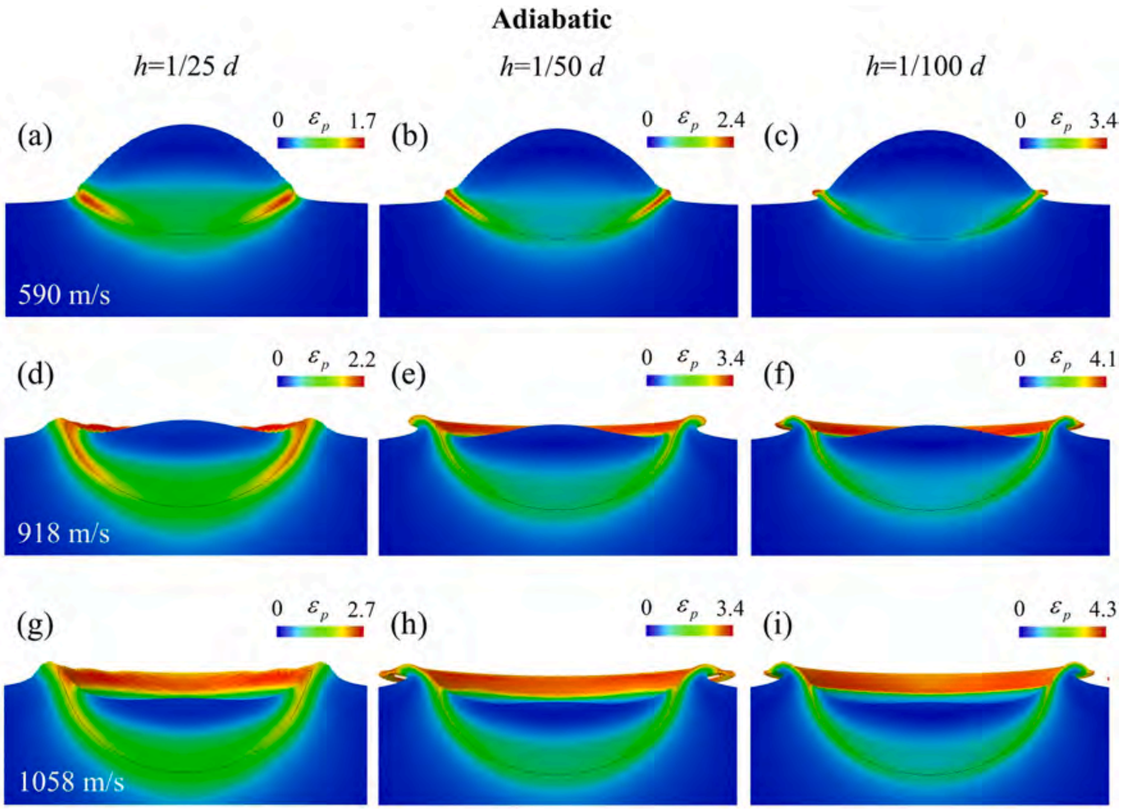

Fig. 8. Particle deformation and equivalent plastic strain field under different velocities and mesh sizes simulated by the proposed model using adiabatic assumption in the analysis.

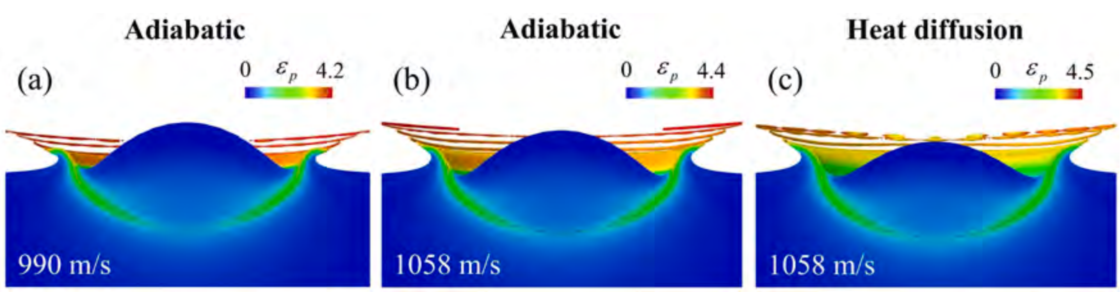

Fig. 9. Unrealistic melting occurring with the mesh size of $h = 1/100$th d: adiabatic analysis at velocities of (a) 918 m/s and (b) 1058 m/s; (c) heat diffusion analysis at velocity of 1058 m/s. The contours represent the equivalent plastic strain field.

where C_1 and C_2 have the units of length to the power of ∇; ∇^2 is the Laplacian operator and $\nabla^n = \left(\nabla^2\right)^{n/2}$. When the higher order gradient terms are neglected and the Pade approximations are utilized, the implicit gradient form can be obtained, as follows:

$$\bar{f}(\mathrm{x}) - C_1 \nabla^2 \bar{f}(\mathrm{x}) = f(\mathrm{x}) \boldsymbol{with} C_1 = l^2, \tag{15}$$

where l is the characteristic length [80] used to couple the deformation responses of the integration points located within a specified distance, thereby establishing the nonlocal spatial interactions. In a 1D case, the implicit form has the same expression as the nonlocal integral formulation by considering a particular Green's function and boundary conditions [81].

However, the standard implicit gradient enhancement does not always fully regularize the problem. Therefore, an over-nonlocal formulation was proposed in [82] to achieve stronger regularization, expressed as:

$$\hat{f}(\mathrm{x}) = m\bar{f}(\mathrm{x}) + (1 - m)f(\mathrm{x}), \tag{16}$$

where $\hat{f}(\mathrm{x})$ will replace $\bar{f}(\mathrm{x})$ to serve as the nonlocal variable, thereby accounting for both local and nonlocal contributions, simultaneously. When $m > 1$, Eq. (16) is regarded as over-nonlocal scheme, and $m = 2$ is commonly used in different over-nonlocal models [46,83] as it can induce significant nonlocal effects.

5.2. Development of nonlocal strategy for CS simulations

Here we considered the weight functions of three distinct approaches of local, standard nonlocal and over-nonlocal for which the distance from central integration point is shown in Fig. 11.

The local method considers only the local variables of central integration point. The standard nonlocal method accounts for local variables of the neighboring integration points, but the central integration point still has the highest weight, which means that the nonlocal variables of

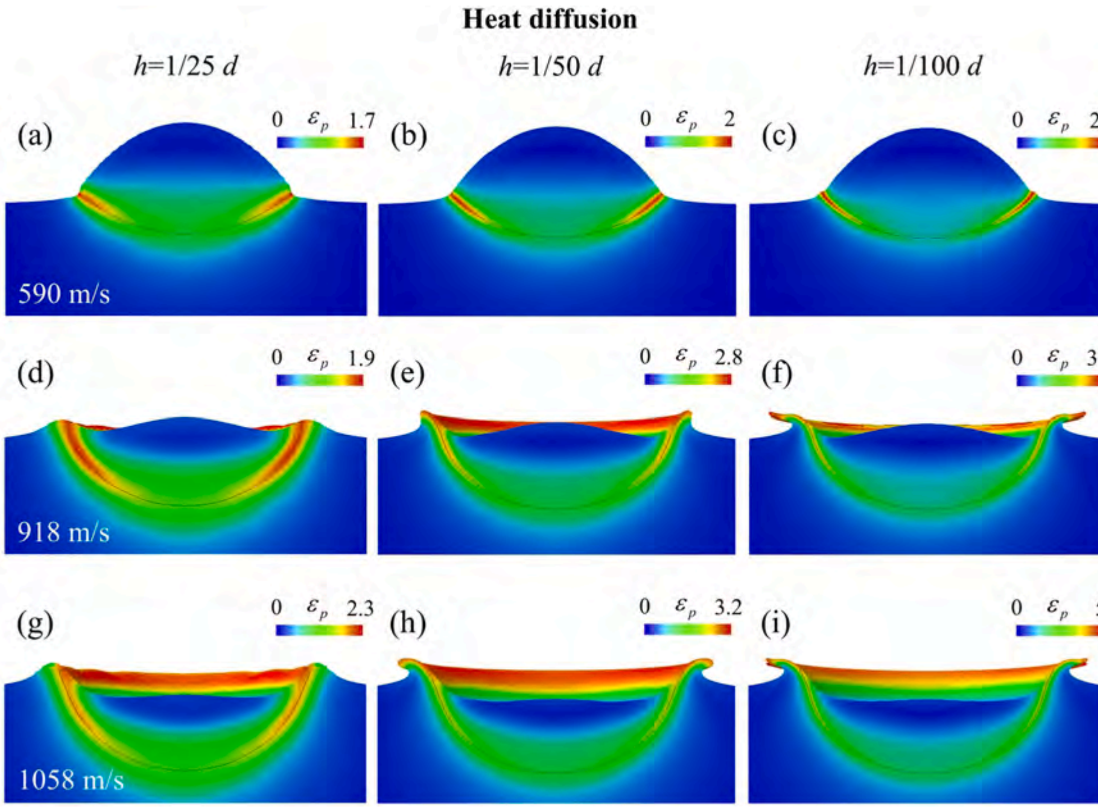

Fig. 10. Particle deformation and equivalent plastic strain field under different velocities and mesh sizes simulated by the proposed model using heat diffusion analysis.

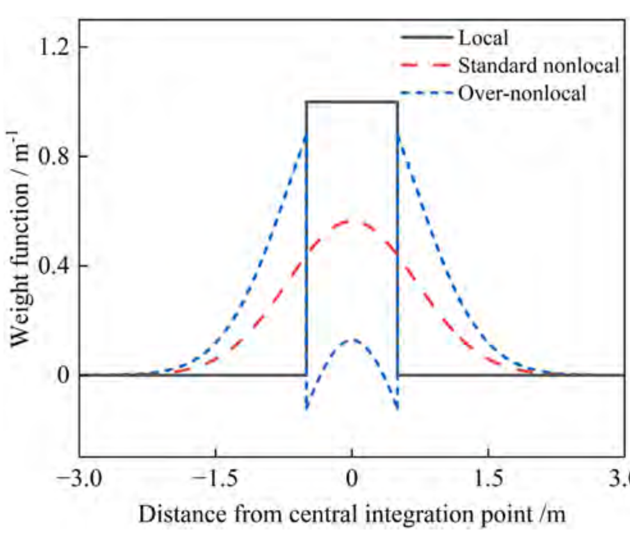

Fig. 11. Wt functions of local, standard nonlocal and over-nonlocal methods for $l = h = 1\boldsymbol{m}$ (Gaussian distribution is used for illustration).

one integration point are still highly dependent on their local variables. The over-nonlocal method presents the lowest weight at the central integration point, which allows the nonlocal variables to be determined by the local variables of the neighboring integration points. Therefore, the over-nonlocal method provides a stronger regularization than the standard nonlocal method [83].

To account for thermal softening in CS simulations, the adiabatic and heat diffusion analyses represent the temperature field calculated by the local method and the standard nonlocal method, respectively. This explains why the heat diffusion analysis mitigated the excessive deformation found in the adiabatic analysis with fine mesh but didn't eliminate it; this observation indicates that the standard nonlocal method (heat diffusion) cannot fully regularize the thermal softening behavior. Thus, the over-nonlocal method can be used for this purpose.

As regards the kinematic issue, when mesh refinement is not possible, the standard nonlocal method effectively reduces mesh dependency by averaging variables across neighboring integration points, leading to more stable and reliable numerical solutions. The equivalent plastic strain and equivalent plastic strain rate can be nonlocalized, so that they are not entirely concentrated in the elements near the particle-substrate interface, thus extending the shear band width and mitigating kinematic issue. The over-nonlocal method was not applied since the equivalent plastic strain and equivalent plastic strain rate must have maximum values at the central integration point to satisfy kinematic rules, otherwise it will lead to the convergence issue.

In summary, for the proposed nonlocal strategy, ε_p and $\dot{\varepsilon}_p$ are replaced by the nonlocal $\overline{\varepsilon}_p$ and $\dot{\overline{\varepsilon}}_p$, whereas T is replaced by the over-nonlocal $\widehat{T}$. Thus, Eq. (1) is reformulated as:

$$\sigma_y = \left[\left(\sigma_{y0} + A\overline{\varepsilon}_p{}^n\right) + \left(\alpha\overline{\varepsilon}_p{}^n + \beta\right)\ln\left(\frac{\dot{\overline{\varepsilon}}_p}{\dot{\varepsilon}_s}\right) + B\ln\left(\frac{\dot{\overline{\varepsilon}}_p}{\dot{\varepsilon}_u}\right)\right]\left(\frac{1 + e^{(T_r - T_{ref})\eta}}{1 + e^{(\widehat{T} - T_{ref})\eta}}\right). \tag{17}$$

5.3. Numerical implementation of the proposed nonlocal strategy

Numerical Implementation of the nonlocal method is challenging due to the need for computationally intensive weighted averaging of field variables across spatial neighborhoods, which also requires careful attention to boundary conditions and numerical stability. For the proposed nonlocal strategy, it is necessary to compute ε_p, $\dot{\varepsilon}_p$ and T simultaneously, all of which can be obtained from γ, according to Eq. (8). VUMAT subroutine can be used to implement the applied implicit gradient enhancement. Specifically, the nonlocal plastic multiplier $\overline{\gamma}$ was analogized to the degree of freedom T' in coupled thermal–displacement analysis [84]. The transient heat transfer equation can be expressed as:

$$k'\nabla^2 T' + r = \rho c'_p \frac{\partial T'}{\partial t}, \tag{18}$$

where k' is the thermal conductivity coefficient and r is the volumetric heat flux. By substituting γ into Eq. (15), the equation is rewritten to provide a clearer analogy with Eq. (18):

$$l^2\nabla^2\overline{\gamma} + \gamma - \overline{\gamma} = 0, \tag{19}$$

Considering $k' = 1$, r can be analogized by as follows:

$$r = \gamma - \overline{\gamma} \boldsymbol{with} \rho c'_p \frac{\partial T'}{\partial t} \rightarrow 0, \tag{20}$$

where c'_p needs to be determined using an iterative approach. In VUMAT, the thermal behavior cannot be directly applied. Alternatively, $W^{Inelastic}$ can be used to define r:

$$r = \frac{Q'\rho\left(W^{Inelastic}_{n+1} - W^{Inelastic}_{n}\right)}{\Delta t}, \tag{21}$$

when $Q' = 1$, and by substituting Eq (19) into Eq (20), $W^{Inelastic}_{n+1}$ can be calculated as:

$$W^{Inelastic}_{n+1} = \frac{(\gamma_n - \overline{\gamma}_n)\Delta t}{\rho} + W^{Inelastic}_{n}. \tag{22}$$

Then, $\overline{\gamma}_{n+1}$ is updated by the current temperature field variable *tempNew*. Thereby $\overline{\varepsilon}_p$, $\dot{\overline{\varepsilon}}_p$ and $\widehat{T}$ can be updated as:

$$\begin{cases} \overline{\varepsilon}_{p,n+1} = \overline{\varepsilon}_{p,n} + \sqrt{\frac{2}{3}}\overline{\gamma}_{n+1} \\ \dot{\overline{\varepsilon}}_{p,n+1} = \sqrt{\frac{2}{3}}\frac{\overline{\gamma}_{n+1}}{\Delta t} \\ \widehat{T}_{n+1} = 2\overline{T}_{n+1} - T_{n+1} \text{with} \overline{T}_{n+1} = \overline{T}_n + \sqrt{\frac{2}{3}}\left[\frac{\overline{\gamma}_{n+1}\left(\sigma_{y,n+1} + \sigma_{y,n}\right)}{2}\right]\frac{Q}{\rho C_p} \end{cases}. \tag{23}$$

A flowchart of the numerical implementation of the proposed nonlocal strategy is provided in Appendix B.

5.4. Simulation results by nonlocal strategy

The same simulation parameters used in Section 4 were utilized to validate the proposed nonlocal strategy. Since the characteristic length affects the numerical results, it can be treated as a material parameter [83]. An iterative approach was employed to determine its value. When the characteristic length was set to 4 μm, the simulated particle morphology demonstrated strong agreement with experimental observations. This finding suggests that the characteristic length for Cu particles can be set to $l = 2/5\,d$ Another nonlocal parameter, $c_p = 0.001$ was introduced to ensure that the function in Eq. (20) approaches zero. The simulation results are shown in Fig. 12.

For the kinematic issue, compared with the analysis without thermal softening, the nonlocal strategy exhibited better match in maximum equivalent plastic strain across different mesh sizes, with consistent shear band localization and nearly identical shear band widths. Although it didn't fully eliminate the mesh sensitivity caused by kinematic issue, the sensitivity was significantly mitigated. On the other hand, for the elliptic problem, the nonlocal strategy strongly regularized the temperature field, resulting in an overall consistent particle deformation and almost identical local jetting across different mesh sizes. It also eliminated the excessive jetting and unrealistic melting that

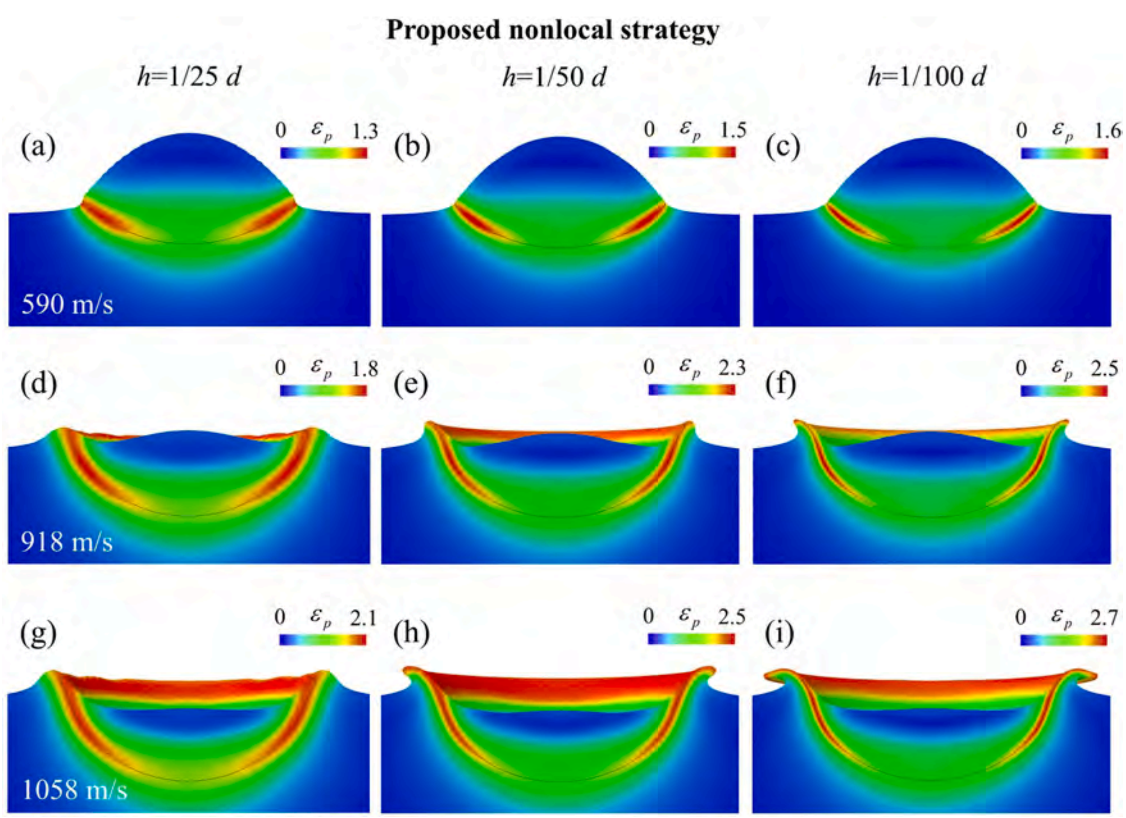

Fig. 12. Particle deformation and equivalent plastic strain field under different velocities and mesh sizes simulated by the proposed model with the nonlocal strategy.

occurred at the mesh size of $h = 1/100\text{th}\ d$ in both the adiabatic and heat diffusion analyses, as shown in Fig. 12(c), (f) and (i).

In summary, the proposed nonlocal strategy was able to mitigate the kinematic issue and eliminate the elliptic problem, while ensuring that the predicted global and local particle deformations remain essentially consistent across different mesh sizes. It also improved the accuracy of shear band localization and the distribution of equivalent plastic strain. Notably, the computational efficiency of the proposed strategy is consistent with that of the other approaches adopted in this study. The computational time of different analysis approaches is provided in Appendix D.

6. Conclusions

In this study, we developed an improved high-fidelity constitutive material model able to predict the deformation of CS deposited particles. The model incorporates strain hardening, strain rate hardening, and thermal softening in describing the flow stress, and its parameters can be readily calibrated with experimental data and implemented within finite element simulations. The validity of the model was established using Cu particles as a representative case; however, its formulation is sufficiently general to be applicable to a broad range of metallic materials. The proposed constitutive material model was validated through single particle deposition simulations, demonstrating strong agreement with experimental data in terms of overall particle deformation, local jetting and flatness of CS deposited particles. Specifically, the model achieved overlapping ratios exceeding 85% and flattening ratio predictions above 95% across a wide velocity range of 590–1058 m/s. It significantly outperforms the MW model at high velocities, reaching a 93.2% overlapping ratio at 1058 m/s compared to 61.8% for the latter.

Furthermore, various simulation approaches, excluding thermal softening, as well as adiabatic and heat diffusion analyses, were employed to examine mesh sensitivity in Eulerian CS simulations. This sensitivity is primarily caused by the intrinsic kinematic issue arising from high-velocity impact and the elliptic problem induced by thermal softening. To overcome mesh dependence, a hybrid nonlocal strategy was successfully implemented combining the conventional nonlocal method to effectively mitigate kinematic issue, and the over-nonlocal approach to address challenges associated with the elliptic problem. The adoption of this nonlocal strategy ensured that both particle deformation and shear band localization were consistently reproduced, regardless of mesh size. The implicit gradient enhancement method facilitated the implementation of nonlocal strategy, offering ease of integration within the VUMAT subroutine and suitability for coupled thermo-mechanical analyses. Notably, it preserved both robustness and computational efficiency, with the computational time variance among the four analysis approaches remaining below 1%.

Overall, the new constitutive material model and nonlocal strategy methods proposed in this work provide a framework that can conveniently be implemented for investigating more complex material behaviors and underlying mechanisms in future studies. Potential applications include CS deposition mechanism, multi-particle impact, and bonding strength criteria, paving the path for improved understanding and broader use of CS.

CRediT authorship contribution statement

Xuanyu Ge: Writing – original draft, Validation, Software, Methodology, Conceptualization. **Linglong Zhou:** Validation, Software, Data curation. **Sara Bagherifard:** Writing – review & editing, Supervision, Resources. **Mario Guagliano:** Writing – review & editing, Supervision, Resources.

Declaration of competing interest

The authors declare that they have no known competing financial interests or personal relationships that could have appeared to influence the work reported in this paper.

Acknowledgments

X.G. acknowledges the Chinese Scholarship Council (CSC) for the financial support (No. 202306290021). L.Z. acknowledges the Chinese Scholarship Council (CSC) for the financial support (No. 202406290022).

Appendix A. Comparison of existing constitutive material models for CS

The advantages and limitations of five representative constitutive models for high-strain-rate impact in CS simulations: Johnson-Cook (JC) [27], Zerilli-Armstrong (ZA) [85], Mechanical threshold stress (MTS) [86], Preston-Tonks-Wallace (PTW) [87], and Ma-Wang (MW) [28], are summarized in Table A.1.

Table A.1
Comparison of existing constitutive material models for CS.

Model	Type	Advantages	Limitations
JC	Empirical	Simple form; easy parameter calibration; widely implemented in FEM software	Lacks physical basis; limited accuracy under extreme conditions
ZA	Semi-physical	Better description of strain-rate and temperature coupling; improved accuracy for FCC metals	Complex parameters calibration; material-dependent formulation;
MTS	Physical	Strong physical foundation; accurate coupling of strain-rate and temperature	Difficult parameters calibration; high computational cost
PTW	Physical	Excellent performance under ultra-high strain rates; suitable for impact and shock problems	Complex formulation; less efficient for standard conditions
MW	Empirical	Easy parameter calibration; high precision; simple numerical implementation	Lacks physical basis; reduced fidelity in high velocities

Compared with these models, the proposed formulation features a simple structure, straightforward numerical implementation, easy parameter calibration, high computational efficiency, and high predictive accuracy. However, like all empirical models such as JC and MW, it lacks a strong physical basis and may lose validity or accuracy under certain conditions. For example, predictive accuracy may decrease at further extreme strain rates (>10^7 s^{-1}) or particle velocities beyond the validated range (>1100m/s); under high temperatures approaching the material's melting point or during phase transformations; and in situations involving dynamic failure or damage mechanisms such as cracking, particle fragmentation, or oxide layer spallation.

Appendix B. Flowchart of the numerical implementation

Herein, a flowchart is provided to clearly illustrate the numerical implementation of the proposed constitutive material model and nonlocal strategy based on the VUMAT subroutine, as shown in Fig. B.1.

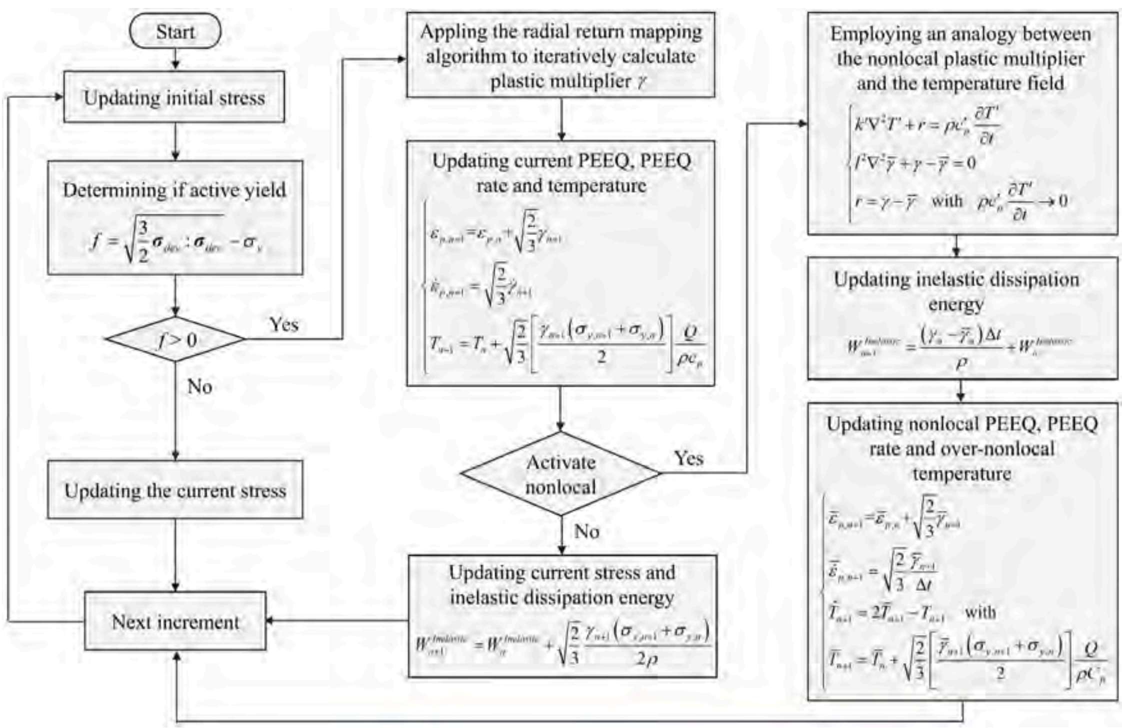

Fig. B.1. Flowchart of the numerical implementation of the proposed constitutive material model and nonlocal strategy.

Appendix C. Temperature evolution during the impact process

The temperature evolution during the impact process of different simulation approaches considering a particle velocity of 918 m/s is shown in Fig. C.1. For the adiabatic analysis, the temperature field was consistent with the PEEQ distribution in Fig. 8, since heat generation depends solely on plastic dissipation, resulting in the most pronounced thermal softening. When heat diffusion was considered, the temperature initially concentrated along the shear band due to the rapid increase of PEEQ at the particle-substrate interface (Fig. C.1(d)). As the impact proceeded, the increase in PEEQ became gradual and the temperature evolution stabilized, while heat diffused from the shear band into the surrounding material, leading to a gradual temperature decrease, as shown in Fig. C.1(e) and (f). Owing to the delocalization of temperature, the nonlocal strategy showed a wider temperature field at the early stage of impact (Fig. C.1(g)). As the impact continued, the temperature increased continuously, and the final temperature field distribution was similar to that of the adiabatic analysis but significantly broader. The results demonstrate that the proposed nonlocal strategy effectively prevents early temperature localization and addresses mesh sensitivity caused by thermal softening.

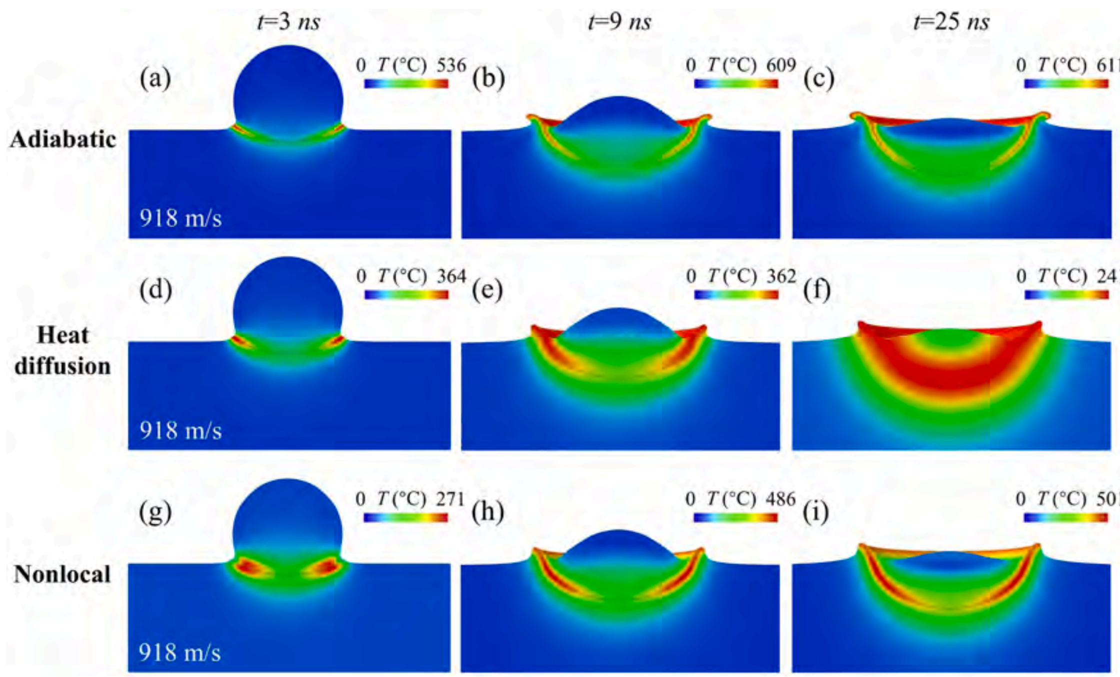

Fig. C.1. Temperature evolution of the adiabatic approach at (a) 3 ns, (b) 9 ns and (c) 25 ns; temperature evolution of the heat diffusion approach at (d) 3 ns, (e) 9 ns and (f) 25 ns; temperature evolution of the nonlocal approach at (g) 3 ns, (h) 9 ns and (i) 25 ns. (918 m/s).

Appendix D. Computational efficiency and numerical stability

All simulations in this study were conducted using the explicit solver in Abaqus. In this framework, the temperature and displacement fields are updated using forward and central difference schemes, respectively. Previous study has demonstrated that explicit simulations maintain robust numerical stability when the time increment is lower than the critical stability limit [84].

The analyses without thermal softening and adiabatic employed *Dynamic step, while the analyses heat diffusion and nonlocal used *Dynamic, temperature–displacement step. For the displacement subproblem, the critical stable time increment is expressed as [84]:

$$\Delta t_u \approx L_{\min}\sqrt{\frac{\rho}{\lambda + 2\mu}} \tag{B.1}$$

where $L_{\min}$ is the mesh size of the smallest element. λ and μ are Lamé constants can be calculated from the elastic modulus and Poisson's ratio. The critical stable time increment for the temperature subproblem is expressed as [84]:

$$\Delta t_T \approx \frac{L_{\min}^2 \rho c_p}{2k} \tag{B.2}$$

When the mesh size is $h = 1/100$th d, the critical stable time increments for the displacement and temperature subproblems are 0.0213 ns and 0.0431 ns, respectively. Although the temperature subproblem is more sensitive to mesh size, its increment remains larger than that of the displacement subproblem even at the finest mesh. Thus, the computational efficiency is primarily governed by the displacement subproblem, consistent with previous studies [84,88]. The computational times for the four analysis approaches at different mesh sizes (918 m/s) are listed in Table D.1. Computational times are comparable across all approaches, with the variation among the four analysis approaches remaining below 1%, indicating that the proposed nonlocal approach does not introduce additional computational cost.

Table D.1
Computational time of four analysis approaches at different mesh sizes (918 m/s).

Mesh size	$h = 1/25\ d$	$h = 1/50\ d$	$h = 1/100\ d$
Without thermal softening (mins)	2.16	21.17	135.43
Adiabatic (mins)	2.17	21.57	135.67
Heat diffusion (mins)	2.17	21.42	136.12
Noncoal strategy (mins)	2.17	21.37	135.85

Data availability

Data will be made available on request.

References

[1] Assadi H, Kreye H, Gärtner F, Klassen T. Cold spraying – A materials perspective. Acta Mater 2016;116:382–407.

[2] Li W, Yang K, Yin S, Yang X, Xu Y, Lupoi R. Solid-state additive manufacturing and repairing by cold spraying: a review. J Mater Sci Technol 2018;34:440–57.
[3] Li W, Cao C, Yin S. Solid-state cold spraying of Ti and its alloys: a literature review. Prog Mater Sci 2020;110:100633.
[4] Poza P, Garrido-Maneiro MÁ. Cold-sprayed coatings: microstructure, mechanical properties, and wear behaviour. Prog Mater Sci 2022;123:100839.
[5] Bagherifard S, Guagliano M. Fatigue performance of cold spray deposits: coating, repair and additive manufacturing cases. Int J Fatigue 2020;139:105744.
[6] Bagherifard S, Monti S, Zuccoli MV, Riccio M, Kondás J, Guagliano M. Cold spray deposition for additive manufacturing of freeform structural components compared to selective laser melting. Mater Sci Eng A 2018;721:339–50.
[7] Yin S, Cavaliere P, Aldwell B, Jenkins R, Liao H, Li W, Lupoi R. Cold spray additive manufacturing and repair: fundamentals and applications. Addit Manuf 2018;21: 628–50.
[8] Bagherifard S, Kondas J, Monti S, Cizek J, Perego F, Kovarik O, Lukac F, Gaertner F, Guagliano M. Tailoring cold spray additive manufacturing of steel 316L for static and cyclic load-bearing applications. Mater Des 2021;203:109575.
[9] Bagherifard S, Heydari Astaraee A, Locati M, Nawaz A, Monti S, Kondás J, Singh R, Guagliano M. Design and analysis of additive manufactured bimodal structures obtained by cold spray deposition. Addit Manuf 2020;33:101131.
[10] Huang C, Chen T, Fu B, Zhang Z, List A, Wiehler L, Klusemann B, Li W, Gärtner F, Klassen T. Ductility and fracture behavior of cold spray additive manufactured zinc. Addit Manuf 2024;89:104310.
[11] Wicaksono RA, Ardeshiri Lordejani A, Bagherifard S. Current trends and future perspective for cold spray metal–ceramic composites. Adv Eng Mater 2025;27: 2401657.
[12] Julien SE, Nourian-Avval A, Liang W, Schwartz T, Ozdemir OC, Müftü S. Bulk fracture anisotropy in cold-sprayed Al 6061 deposits. Eng Fract Mech 2022;263: 108301.
[13] Sayahlatifi S, Zaiemyekeh Z, Shao C, McDonald A, Hogan JD. Micromechanical damage analysis of Al–Al_2O_3 composites via cold-spray additive manufacturing. Int J Mech Sci 2023;259:108573.
[14] Huang C, Arseenko M, Zhao L, Xie Y, Elsenberg A, Li W, Gärtner F, Simar A, Klassen T. Property prediction and crack growth behavior in cold sprayed Cu deposits. Mater Des 2021;206:109826.
[15] Hutasoit N, Javed MA, Rashid RAR, Wade S, Palanisamy S. Effects of build orientation and heat treatment on microstructure, mechanical and corrosion properties of Al6061 aluminium parts built by cold spray additive manufacturing process. Int J Mech Sci 2021;204:106526.
[16] Akin S, Lee S, Jo S, Ruzgar DG, Subramaniam K, Tsai J-T, Jun MB-G. Cold spray-based rapid and scalable production of printed flexible electronics. Addit Manuf 2022;60:103244.
[17] An S, Joshi B, Yarin AL, Swihart MT, Yoon SS. Supersonic cold spraying for energy and environmental applications: one-step scalable coating technology for advanced micro- and nanotextured materials. Adv Mater 2020;32:1905028.
[18] Li W, Yang J, Zhang Z, Xie Y, Huang C. High ductility induced by twin-assisted grain rotation and merging in solid-state cold spray additive manufactured Cu. J Mater Sci Technol 2025;214:11–5.
[19] Chen C, Xie Y, Yin S, Li W, Luo X, Xie X, Zhao R, Deng C, Wang J, Liao H, Liu M, Ren Z. Ductile and high strength Cu fabricated by solid-state cold spray additive manufacturing. J Mater Sci Technol 2023;134:234–43.
[20] Panova V, Schuh CA. Towards a quantitative understanding of bonding in supersonic single particle impacts: a three-dimensional FIB-SEM exploration. Acta Mater 2024;276:120105.
[21] Lucas TJ, Schuh CA. A single particle impact study on the effects of substrate strength and ductility on adhesion in cold spray. Int J Mech Sci 2025;303:110676.
[22] Yin S, Hassani M, Xie Q, Lupoi R. Unravelling the deposition mechanism of brittle particles in metal matrix composites fabricated via cold spray additive manufacturing. Scr Mater 2021;194:113614.
[23] Nastic A, Jodoin B. Evaluation of heat transfer transport coefficient for cold spray through computational fluid dynamics and particle in-flight temperature measurement using a high-speed IR camera. J Therm Spray Technol 2018;27: 1491–517.
[24] Assadi H, Gärtner F, Stoltenhoff T, Kreye H. Bonding mechanism in cold gas spraying. Acta Mater 2003;51:4379–94.
[25] Fardan A, Berndt CC, Ahmed R. Numerical modelling of particle impact and residual stresses in cold sprayed coatings: a review. Surf Coat Technol 2021;409: 126835.
[26] Wang Q, Ma N, Luo X, Li C. Towards better understanding supersonic impact-bonding behavior of cold sprayed 6061-T6 aluminum alloy based on a high-accuracy material model. Addit Manuf 2021;48:102469.
[27] Johnson GR, Cook WH. Fracture characteristics of three metals subjected to various strains, strain rates, temperatures and pressures. Eng Fract Mech 1985;21:31–48.
[28] Wang Q, Ma N, Takahashi M, Luo X, Li C. Development of a material model for predicting extreme deformation and grain refinement during cold spraying. Acta Mater 2020;199:326–39.
[29] Chakrabarty R, Song J. A modified Johnson–Cook material model with strain gradient plasticity consideration for numerical simulation of cold spray process. Surf Coat Technol 2020;397:125981.
[30] Cormier Y, Dupuis P, Jodoin B, Ghaei A. Finite element analysis and failure mode characterization of pyramidal fin arrays produced by masked cold gas dynamic spray. J Therm Spray Technol 2015;24:1549–65.
[31] Henao J, Bolelli G, Concustell A, Lusvarghi L, Dosta S, Cano IG, Guilemany JM. Deposition behavior of cold-sprayed metallic glass particles onto different substrates. Surf Coat Technol 2018;349:13–23.
[32] Xie J, Nélias D, Walter-Le Berre H, Ogawa K, Ichikawa Y. Simulation of the cold spray particle deposition process. J Tribol 2015;137:041401.
[33] Ge X, Ma Y, Zhou L, Li W. Modelling the anisotropic fracture behaviour of cold spray additive manufactured 6061 aluminium alloy deposits based on the phase field method. Addit Manuf 2024;79:103932.
[34] Weiller S, Delloro F. A numerical study of pore formation mechanisms in aluminium cold spray coatings. Addit Manuf 2022;60:103193.
[35] Ardeshiri Lordejani A, Colzani D, Guagliano M, Bagherifard S. An inclusive numerical framework to assess the role of feedstock features on the quality of cold spray deposits. Mater Des 2022;224:111374.
[36] Song X, Jin X, Zhai W, Tan AW, Sun W, Li F, Marinescu I, Liu E. Correlation between the macroscopic adhesion strength of cold spray coating and the microscopic single-particle bonding behaviour: simulation, experiment and prediction. Appl Surf Sci 2021;547:149165.
[37] Li W, Wang X, Yin S, Xu S. Influence of particle initial temperature on high velocity impact process in cold spraying. Procedia Env Sci 2012;12:298–304.
[38] Wang F, Li W, Yu M, Liao H. Prediction of critical velocity during cold spraying based on a coupled thermomechanical eulerian model. J Therm Spray Technol 2014;23:60–7.
[39] Chen J, Hawlader B, Roy K, Pike K. A nonlocal eulerian-based finite-element approach for strain-softening materials. Comput Geotech 2023;154:105114.
[40] Wang Z, Kong D, Zhu Z, Liu B, Zhao M, Li X, Ren Q, Li L. Investigation of cavitating jet erosion using eulerian–Lagrangian modeling. Int J Mech Sci 2025;300:110457.
[41] Longère P. Adiabatic shear banding assisted dynamic failure: some modeling issues. Mech Mater 2018;116:49–66.
[42] Zhong J, Qu F, Sun D, Liu Q, Wang Q, Bai J. Low-frequency unsteadiness mechanisms of unstart flow in an inlet with rectangular-to-elliptical shape transition under off-design condition at a mach number of 4. J Fluid Mech 2024; 991:A9.
[43] Liu X, Osher S, Chan T. Weighted essentially non-oscillatory schemes. J Comput Phys 1994;115:200–12.
[44] Poh LH, Swaddiwudhipong S. Gradient-enhanced softening material models. Int J Plast 2009;25:2094–121.
[45] Aravas N, Xenos S. Implicit vs explicit gradient plasticity models: do they always remove mesh dependence in softening materials? Int J Solids Struct 2023;281: 112415.
[46] Xue D, Lü X, Lim K, Buscarnera G. Nonlocal implicit gradient enhancements for strain localization informed by controllability criteria for plastic solids. Comput Methods Appl Mech Eng 2023;415:116275.
[47] Dolci S, Carney KS, Bois PD, Revilock D, Ruggeri C, Kan C. Novel method in the modeling of adiabatic shear bands in ballistic impact: an application on Inconel 718 alloy. Int J Impact Eng 2023;182:104763.
[48] Berger-Vergiat L, Chen X, Waisman H. Explicit and implicit methods for shear band modeling at high strain rates. Comput Mech 2019;63:615–29.
[49] Shi J, Guan L, Zhuang D, Chen X, Ling D. Fault rupture propagation in soil with intercalation using nonlocal model and softening modulus modification. J Rock Mech Geotech Eng 2023;15:2973–93.
[50] Vignjevic R, Djordjevic N, Gemkow S, De Vuyst T, Campbell J. SPH as a nonlocal regularisation method: solution for instabilities due to strain-softening. Comput Methods Appl Mech Eng 2014;277:281–304.
[51] Peerlings RHJ, de Borst R, Brekelmans WAM, de Vree JHP. Gradient enhanced damage for quasi-brittle materials. Int J Numer Methods Eng 1996;39:3391–403.
[52] Engelen RAB, Geers MGD, Baaijens FPT. Nonlocal implicit gradient-enhanced elasto-plasticity for the modelling of softening behaviour. Int J Plast 2003;19: 403–33.
[53] Poh LH, Swaddiwudhipong S. Over-nonlocal gradient enhanced plastic-damage model for concrete. Int J Solids Struct 2009;46:4369–78.
[54] Chen Y, Liu E, Cai Z. Nonlocal binary-medium constitutive model for quasibrittle materials: a framework with implicit gradient enhancement. Comput Geotech 2026;192:107885.
[55] Rosenbusch SM, Balzani D, Unger JF. Regularization of softening plasticity models for explicit dynamics using a gradient-enhanced modified Johnson–Holmquist model. Int J Impact Eng 2025;198:105209.
[56] Ahad FR, Enakoutsa K, Solanki KN, Bammann DJ. Nonlocal modeling in high-velocity impact failure of 6061-T6 aluminum. Int J Plast 2014;55:108–32.
[57] Seupel A, Hütter G, Kuna M. An efficient FE-implementation of implicit gradient-enhanced damage models to simulate ductile failure. Eng Fract Mech 2018;199: 41–60.
[58] Regazzoni G, Kocks UF, Follansbee PS. Dislocation kinetics at high strain rates. Acta Met 1987;35:2865–75.
[59] Dowding I, Schuh CA. Metals strengthen with increasing temperature at extreme strain rates. Nature 2024;630:91–5.
[60] Rusinek A, Rodríguez-Martínez JA. Thermo-viscoplastic constitutive relation for aluminium alloys: modeling of negative strain rate sensitivity and viscous drag effects. Mater Des 2009;30:4377–90.
[61] Liu R, Salahshoor M, Melkote SN, Marusich T. A unified material model including dislocation drag and its application to simulation of orthogonal cutting of OFHC copper. J Mater Process Technol 2015;216:328–38.
[62] Follansbee PS, Kocks UF. A constitutive description of the deformation of Cu based on the use of the mechanical threshold stress as an internal state variable. Acta Met 1988;36:81–93.
[63] Lea LJ, Jardine AP. Characterisation of high rate plasticity in the uniaxial deformation of high purity Cu at elevated temperatures. Int J Plast 2018;102: 41–52.
[64] Chen T, Wen M, Cui H, Guo J, Wang C. Hot deformation behavior and processing maps of pure copper during isothermal compression. Mater (Basel) 2023;16:3939.

[65] Li W, Zhang X, Kou H, Wang R, Fang D. Theoretical prediction of temperature dependent yield strength for metallic materials. Int J Mech Sci 2016;105:273–8.

[66] Wu Z, Bei H, Pharr GM, George EP. Temperature dependence of the mechanical properties of equiatomic solid solution alloys with face-centered cubic crystal structures. Acta Mater 2014;81:428–41.

[67] Li W, Liao H, Li C, Li G, Coddet C, Wang X. On high velocity impact of micro-sized metallic particles in cold spraying. Appl Surf Sci 2006;253:2852–62.

[68] Li W, Zhang D, Huang C, Yin S, Yu M, Wang F, Liao H. Modelling of impact behaviour of cold spray particles: review. Surf Eng 2014;30:299–308.

[69] Li W, Yang K, Yin S, Guo X. Numerical analysis of cold spray particles impacting behavior by the eulerian method: a review. J Therm Spray Technol 2016;25:1441–60.

[70] Yu M, Li W, Wang F, Liao H. Finite element simulation of impacting behavior of particles in cold spraying by eulerian approach. J Therm Spray Technol 2012;21:745–52.

[71] Tiamiyu AA, Schuh CA. Particle flattening during cold spray: mechanistic regimes revealed by single particle impact tests. Surf Coat Technol 2020;403:126386.

[72] Tiamiyu AA, Sun Y, Nelson KA, Schuh CA. Site-specific study of jetting, bonding, and local deformation during high-velocity metallic microparticle impact. Acta Mater 2021;202:159–69.

[73] Ge X, Ma Y, Fu N, Zhang W, Wang Z. A generalized ductile phase field model for fracture behavior of three-dimensional metal structures. Int J Appl Mech 2023;15:2350046.

[74] Soares GC, Hokka M. The Taylor–Quinney coefficients and strain hardening of commercially pure titanium, iron, copper, and tin in high rate compression. Int J Impact Eng 2021;156:103940.

[75] Salehi SD, Kingstedt O. Critical assessment and demonstration of high-emissivity coatings for improved infrared signal quality for Taylor–Quinney coefficient experimentation. Int J Impact Eng 2023;178:104593.

[76] Ming L, Pantalé O. An efficient and robust VUMAT implementation of elastoplastic constitutive laws in Abaqus/explicit finite element code. Mech Ind 2018;19:308.

[77] Tang Q, Veysset D, Assadi H, Ichikawa Y, Hassani M. Strength gradient in impact-induced metallic bonding. Nat Commun 2024;15:9630.

[78] Yin S, Wang X, Suo X, Liao H, Guo Z, Li W, Coddet C. Deposition behavior of thermally softened copper particles in cold spraying. Acta Mater 2013;61:5105–18.

[79] Pijaudier-Cabot G, Bažant ZP. Nonlocal damage theory. J Eng Mech 1987;113:1512–33.

[80] Ge X, Zhou L, Ying Y, Bagherifard S, Guagliano M. Combining phase field method and critical distance theory for predicting fatigue life of notched specimens. Int J Mech Sci 2024;282:109608.

[81] Peerlings RHJ, Geers MGD, de Borst R, Brekelmans WAM. A critical comparison of nonlocal and gradient-enhanced softening continua. Int J Solids Struct 2001;38:7723–46.

[82] Di Luzio G, Bažant ZP. Spectral analysis of localization in nonlocal and over-nonlocal materials with softening plasticity or damage. Int J Solids Struct 2005;42:6071–100.

[83] Chen J, Hawlader B, Roy K, Pike K. Comparison of local and nonlocal regularization approaches in eulerian-based finite element analyses. Comput Geotech 2023;162:105617.

[84] Ge X, Zhou L, Bagherifard S, Guagliano M. A simple and efficient implementation of explicit phase field method in ABAQUS to address complex three-dimensional fracture problems. Eng Fract Mech 2025;323:111222.

[85] Henao J, Bolelli G, Concustell A, Lusvarghi L, Dosta S, Cano IG, Guilemany JM. Deposition behavior of cold-sprayed metallic glass particles onto different substrates. Surf Coat Technol 2018;349:13–23.

[86] Banerjee B. The Mechanical Threshold stress model for various tempers of AISI 4340 steel. Int J Solids Struct 2007;44:834–59.

[87] Preston DL, Tonks DL, Wallace DC. Model of plastic deformation for extreme loading conditions. J Appl Phys 2003;93:211–20.

[88] Ying Y, Feng Y, Huang W, Yao X. A thermo-mechanical phase field fracture model considering solid–liquid transition. Eng Fract Mech 2026;338:112025.